# Nondestructive quantitative measurement for precision quality control in additive manufacturing using hyperspectral imagery and machine learning.

YAN, Y., REN, J., SUN, H. and WILLIAMS, R.

2024

# Nondestructive Quantitative Measurement for Precision Quality Control in Additive Manufacturing Using Hyperspectral Imagery and Machine Learning

Yijun Yan, *Member, IEEE*, Jinchang Ren, *Senior Member, IEEE*, He Sun, and Robert Williams

***Abstract*—Measuring the purity of the metal powder is essential to maintain the quality of additive manufacturing products. Contamination is a significant concern, leading to cracks and malfunctions in the final products. Conventional assessment methods focus more on physical integrity rather than material composition and can be time-consuming. By capturing spectral data from a wide frequency range along with the spatial information, hyperspectral imaging (HSI) can detect minor differences in terms of temperature, moisture, and chemical composition to tackle this challenge. In this article, we explore the application of HSI in conjunction with machine learning for nondestructive inspection of metal powders. By employing near-infrared and visible HSI cameras, we introduce the utilization of HSI for this purpose. We delve into the technical challenges encountered and present detailed solutions through three case studies, including the establishment of a spectral dictionary, contamination detection, and band selection analysis. Our experimental results demonstrate the immense potential of HSI and its synergy with machine learning for nondestructive testing in powder metallurgy, particularly in meeting the requirements of industrial manufacturing environments.**

***Index Terms*—3-D printing, additive manufacturing (AM), hyperspectral imaging (HSI), metal powder, nondestructive testing (NDT), quality control.**

Manuscript received 31 May 2023; revised 31 October 2023; accepted 27 March 2024. This work was supported by Carpenter Additive, LPW Technology, Ltd., who also provided the metal samples in our case studies. The work of He Sun was supported by the National Natural Science Foundation of China under Grant 62301534. Paper no. TII-23-1952. *(Corresponding author: Jinchang Ren.)*

Yijun Yan is with the National Subsea Centre, Robert Gordon University, AB21 0BH Aberdeen, U.K., and also with the School of Science and Engineering, University of Dundee, DD1 4HN Dundee, U.K. (e-mail: yijun.yan@ieee.org).

Jinchang Ren is with the National Subsea Centre, Robert Gordon University, AB21 0BH Aberdeen, U.K. (e-mail: j.ren@rgu.ac.uk).

He Sun is with the Key Laboratory of Computational Optical Imaging Technology, Aerospace Information Research Institute, Chinese Academy of Sciences, Beijing 100094, China (e-mail: sunhe@aircas.ac.cn).

Robert Williams is with the LPW Technology, Ltd., WA8 0GU Liverpool, U.K. (e-mail: rwilliams@carpenteradditive.com).

Color versions of one or more figures in this article are available at https://doi.org/10.1109/TII.2024.3384609.

## I. Introduction

TAKING advantage of 3-D printing, additive manufacturing (AM) has become one of the most significant manufacturing industries due to its capacity to save time and cost, reduce waste, and reuse material during the printing process, and streamline supply chains. Nowadays, collaboration between the AM and other major industries, such as aerospace, medicine, automotive, and architecture, is growing progressively. In the next five years, the AM market is projected to expand from $ 51 billion to $ 120 billion [1].

During the 3-D printing process, a 3-D object will be formed by layering the powder material. Typically, 5%–10% of raw material in the powder bed [2], [3] will be used to make a component in AM, which means a significant portion of the material remains unmelted and is often recycled in the collector chamber for reuse in subsequent builds. However, every time the material is reused, there is a risk of contamination. Contaminants can arise from the degradation of the material itself or from external sources in processes, such as oxidation, moisture, corrosion, and creep [4], [5], [6], [7], [8], [9], [10], [11].

Oxidation of reused powder leads to oxygen pickup and oxide layer formation on particles, altering surface chemistry and composition [4]. Higher oxygen content enables oxide phase nucleation during printing, which impairs the strength, ductility, and fatigue resistance of the formed component [5]. As for moisture, it introduces hydrogen contamination in reactive alloy powders, e.g., Ti and Al alloys. Absorbed hydrogen causes porosity, acting as crack initiation sites, degrading tensile and fatigue properties [6]. In addition, corrosion alters the surface composition of powders through a preferential dissolution of more reactive elements. The enrichment of less noble residues affects reactivity and the localization of galvanic corrosion during processing and in end-use [7]. Finally, creep causes composition changes via diffusion and rearrangement of alloying elements at high temperatures. This can create localized compositional variations, leading to property mismatches and weakened interfaces prone to failure [8].

When such degradation occurs on the particle surface, these particles are incorporated into subsequent build layers, and the difference in material composition can result in crack propagation points. In critical industries, such as aerospace and medical

sector, precise control of metal powder composition is crucial, as even minor variations can induce noticeable defects by altering the microstructure evolution during the 3-D printing [9], [10]. By mixing different alloy powders, compositional gradients at interparticle boundaries can be generated, which will disrupt the diffusion and the growth of desired phases [11]. Contamination caused by foreign particle provides heterogeneous nucleation sites that change the solidification patterns and dendrite morphology. The resulting microsegregation and nonequilibrium structures reduce the ductility and fatigue life [2]. Therefore, it is essential to develop a nondestructive technique for identifying powder contamination, enabling nondestructive quality assessment of the powders before deciding their suitability for reuse [12].

Currently, typical methods for inspection of 3-D printing materials include visual inspection, ultrasonic testing, thermal imaging, metallography, and X-ray computed tomography (XCT) [13], as detailed in the following text. Visual inspection is a quick and low-cost inspection method where an extra instrumentation is not needed. However, it is less effective for metallurgical condition assessment due to two main reasons. One is the similar color properties of the commonly used metal powders, including TI-6AL4V, AlSi10Mg, Tungsten, M300 Steel, and IN718, and the other is the micron-level particle, which is too small to be easily distinguished by human eyes.

Ultrasonic testing has been widely used to inspect internal defects of metal components. It employs a transmitting probe that transmits ultrasonic waves through the component and then emits various reflected signals when encountering different surfaces. The difference between the transmission times of various signals can help to reveal faults, e.g., pores and cracks [14]. Recently, laser ultrasonic inspection has been developed for real-time AM monitoring. It generates the ultrasonic waves by laser pulse and detects the reflected signal with a laser interferometer. However, ultrasonic testing struggles with nonsmooth and complicated surfaces, requiring the treating of surfaces to eliminate the influence of surface roughness [15].

Thermal imaging is mostly carried out by infrared cameras for temperature measurement, where any physical changes and defects during the manufacturing will affect the heat conduction in the workpieces, and present a higher temperature response in infrared images [16]. However, making accurate measurement relies on a high-sensitive and expensive infrared camera [17]. A comprehensive calibration is also needed depending on the ambient conditions and materials.

XCT is an imaging technique that reconstructs the 3-D structure of an object by capturing several X-ray pictures around a rotating axis. It can expose the internal structure of a metallurgical product, allowing for the detection of defects, such as cracks, porosity, inclusions, and density variations [18]. Since XCT relies on the X-ray penetration of the object to be scanned, larger size of the object will reduce the maximum possible magnification of the scan and lead to a decreased spatial resolution [19]. Although this issue can be mitigated by stitching multiple locally tomographic images to form larger tomograms, the results can be still skewed and make it a challenge in detecting small defects [20].

Metallography, also known as optical microscopy, captures several 2-D images by optical light microscope and then stitches them together to create and record the whole cross section of the workpieces [21], enabling a very high precision for pore detection. However, its experimental setup and calibration are very complex, including the selection of lens magnification and the number of captured images under different magnification levels. Also, manual focus adjustment and location choice during the data capturing may cause human errors and increase uneconomical manpower [22].

Most of the aforementioned techniques extract information about the physical integrity of the as-built components rather than the material composition of the metal powders. In this context, hyperspectral imaging (HSI), an emerging technique that combines spectroscopy with digital imaging, can provide a novel insight to fill this gap.

Conventional multispectral systems, e.g., color cameras, use the red (R), green (G), and blue (B) as three channels to collect information. HSI, in contrast, captures intensities over a continuous spectral range in a series of very narrow wavebands. Each pixel at the spatial coordinates of $(x, y)$ contains the rich spectral information as a continuous spectrum. Depending on the sensor properties and settings, this can entail hundreds of wavebands. The data are stored in a 3-D data cube, often referred to as a hypercube, where for each wavelength, it will form a full-resolution spatial image.

HSI has been widely applied to remote sensing for land mapping [23], precision agriculture [24], and mineral exploration [25]. Due to the recent advances in imaging technology, HSI has become more popular for industrial applications, such as peatness prediction in the malted barley for Whisky manufacturing [26], nondestructive testing (NDT) of carbon fiber reinforced polymer remanufacturing [27], and corrosion detection in nuclear packages [28]. The popularity derives from the nondestructive nature of HSI, where samples can be analyzed chemometrically without altering their physical integrity. A second advantage is the comprehensive data acquisition even in real time. It will not be limited by the environmental temperature and geometry of the object, making it a unique and effective solution for nondestructive inspection far beyond conventional techniques. It is expected that this will subsequently reduce the costs and environmental impact associated with the production of unqualified products. As a result, HSI poses the great potential of a real-time chemometric analysis tool that can seamlessly be integrated into the processing chain of industrial production.

Due to the constrained lab environment, it was infeasible to accurately obtain metal powders with defined levels of contamination. Instead, the mixtures of different pure metals served as simplified proxies for contamination in this study. We aimed to evaluate whether our proposed approach could detect anomalies within the composed metal powders so as to demonstrate the proof-of-concept in smart sensing and quality control of compositional variations in AM. To achieve this, we carried out three experimental case studies, which included spectral dictionary establishment of metal powders, detection of contamination, and band selection.

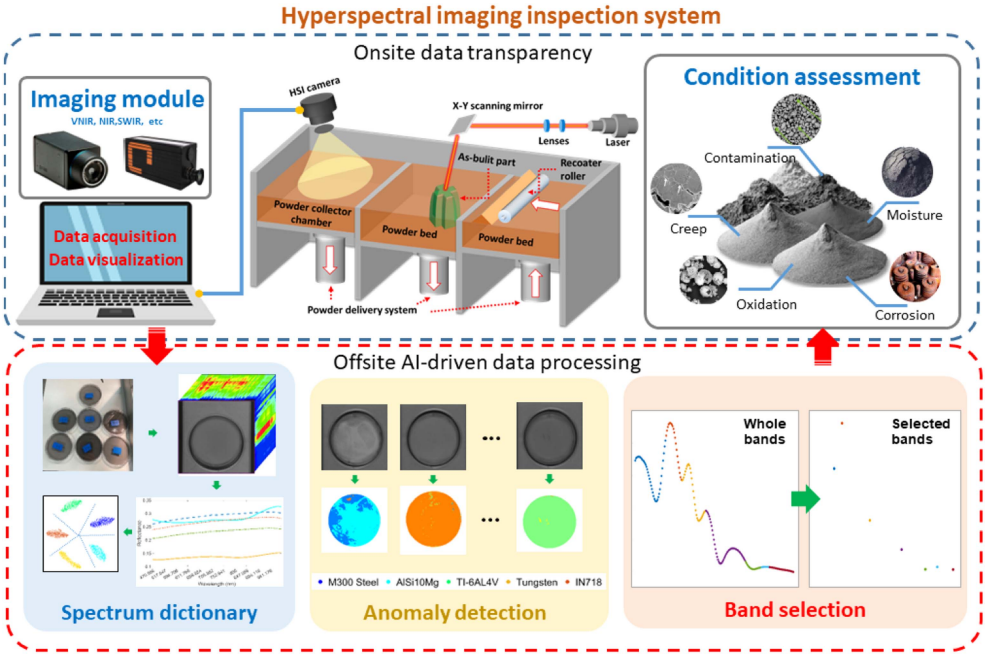


Fig. 1. HSI inspection system for powder metallurgy.

As the spatial resolution of HSI camera is in millimeters, in comparison with the particle size of metal powders in microns, each pixel will contain hundreds to thousands of metal particles. For the accurate mapping of the ground truth (GT), a high-resolution microscope is needed. Since the microscope can only cover a small region, this will require numerous operations to capture the full scene, thus increasing the processing time and the difficulty to keep the distribution consistency of the powders. Thus, this has led to a huge challenge of the uncertainty in data annotation for GT mapping, for which HSI and machine learning are combined to detect the contamination as a special classification problem, using the spectral dictionary established from the original samples to discriminate the contamination.

Although HSI contains rich spectral information, the high dimensionality is also a big challenge that affects the computational efficiency and difficulty in practical deployment caused by the heavy device cost [29]. Herein, a new proximity ranking-based band selection (PRBS) approach is proposed to enable filter the redundant bands while preserving the representative ones in the NDT of metal powders.

The major contributions of this article are highlighted as follows.

1) To the best of our knowledge, we are the first to propose an HIS-based inspection framework for metal powder characterization, integrating onsite transparent data collection with offsite AI-driven data processing to serve AM.
2) We demonstrated the ability of HSI and machine learning to detect the contamination in mixed metal powder samples using a spectral dictionary approach.
3) We introduced a new band selection method called PRBS to reduce HSI data redundancy while maintaining the most representative information.

The rest of this article is organized as follows. Section II describes the concept of the HIS-based inspection system. Section III discusses the way to data acquisition and data processing in this system. Section IV details the three case studies. Finally, Section V concludes this article.

## II. HSI Inspection System

The concept of the HSI inspection system for AM is summarized in Fig. 1, which is composed of two interactive modules, i.e., onsite data transparency and offsite AI-driven data processing. For data-intensive applications, data transparency is essential for evidence-based decision making through proper information collection and evaluation of its effect and usefulness [30]. In our HSI inspection system, both imaging module and condition assessment are accessible to users for onsite data transparency. In the imaging module, any optical sensor, such as visible (VIS), near-infrared (NIR), and short-wave infrared HSI cameras, can be adopted. The acquired information flow will be transferred from onsite to offsite for data processing and analysis. In condition assessment, the outcomes of data processing and analysis will assist the metallurgical experts in understanding the state of metal powders, allowing them to make more informed decisions.

Within the data processing techniques, three core streams are covered, i.e., dictionary building, anomaly detection, and band selection. Dictionary building is a vital step for learning the spectral information from the original metal powders, where data calibration and enhancement of the acquired data are needed to produce high-quality data for easy understanding and improved analysis in following-on modules. In general, spectral calibration is an essential step to normalize the captured spectrum. According to the practical needs of different NDT tasks, spectral

correction and spatial denoising are needed for improving the data quality. For large objects, image registration and stitching are also essential to tackle the limitation of the field of view and cover the whole surface of the object.

One of the biggest issues in analyzing hyperspectral data is the large number of variables involved, leading to the curse of dimensionality or the Hughes phenomenon [26]. A high number of variables necessitates a considerable number of samples, thus the corresponding memory and processing capacity, and may potentially result in overfitting of the AI models during model training. To address this issue, band selection is the main technique used in our system for mining HSI data. Band selection is beneficial for dimension reduction and more effectively data characterization. Moreover, selecting fewer bands can lead to the development of a bespoke multispectral camera that can capture the critical spectral information while reducing the heavy cost associated with a normal HSI camera for more feasible on-site deployment.

Machine learning algorithms, such as the support vector machine (SVM), random forest, and neural network, have been widely applied to a wide range of industrial applications [26], [27]. Combining dictionary building, band selection, and classification can provide an automatic anomaly detection mechanism for detecting the defects of contamination, moisture, corrosion, oxidation, and creep in the metal powder.

In summary, the proposed HSI inspection system can be employed for better condition assessment of metal powders, helping on-site operators make more efficient manufacturing strategies and improve quality control in 3-D printing.

## III. Materials and Methodologies

In this section, the standard progress of data acquisition in the lab environment and data preprocessing techniques are introduced. Those techniques are not only used in this work but also applicable in many other HSI applications.

### A. Data Acquisition

In our case studies, HSI cubes were collected using a visible-near infrared (VIS, 400–950 nm) camera and a near-infrared (NIR, 950–1700 nm) camera in a push-broom scanning configuration (see Fig. 2). Two 20-W Tungsten halogen lights were used for illumination. The samples were raster scanned with a working distance of 25 cm beneath the cameras using a motorized stage at a consistent speed of 16 mm/s to build up the HSI datacubes with two spatial dimensions and a spectral one.

The VIS camera comprised a Hamamatsu ORCA-03G CCD detector and Specim V8E spectrograph, providing 2 nm spectral resolution. The four times binning was applied during VIS acquisition for reduced noise and enhanced sensitivity, resulting in 336 pixels per line and 256 spectral responses per pixel. The NIR imaging utilized an Innospec RedEye 1.7 camera with 10 nm spectral resolution without binning, resulting in 256 spectral bands and 320 spatial pixels per line. Further details of the hyperspectral systems are provided in Table I. Fig. 3(a) and (b) shows the average spectral profiles of the five original

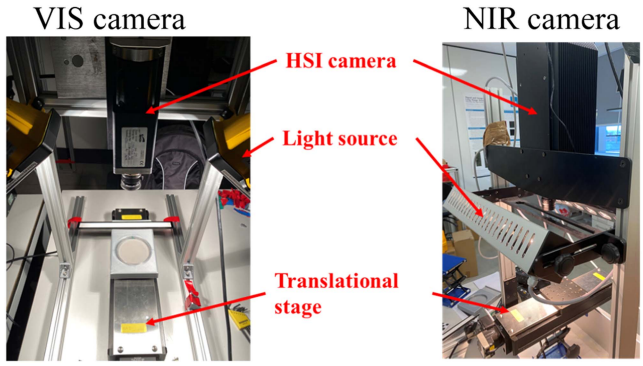


Fig. 2. Camera settings in the lab environment.

TABLE I
Technical Details of Two HSI Cameras for Data Acquisition

| | NIR camera InnoSpec RedEye 1.7 | VIS/VNIR camera Hammatsu |
|---|---|---|
| Spectral range | 950–1700 nm | 400–1000 nm |
| Pixels | 320 * 256 | 336 * 256 |
| Spectral resolution | 10 nm | 2 nm |

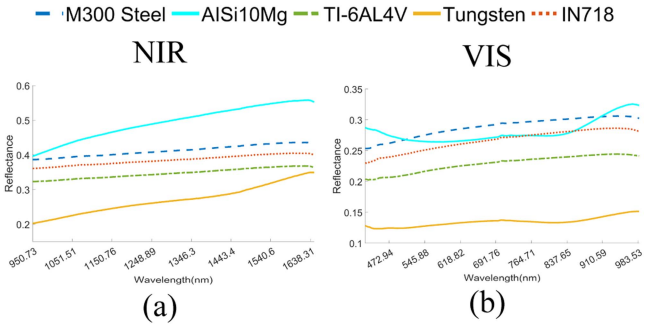


Fig. 3. Spectral profiles of five original samples using the (a) NIR and (b) VIS cameras.

metal powders over the entire spectral bands of NIR and VIS. Aluminum and Tungsten exhibit distinct spectral profiles, while M300 Steel, TI-6AL4V, and IN718 have similar trends despite varying intensities.

Fig. 4 presents microscopic images of the five original metal powders acquired using a 100× Apex microscope. All powder types exhibit approximately spherical morphologies, with some minor variations in particle size and shape observed. As the primary focus of this research was demonstrating the capability of HSI and machine learning for anomaly detection in metal powders, we made a simplifying assumption of uniform spherical particles. This allowed establishing an initial methodology without modeling complex particle factors.

During the data acquisition, the powder samples were scanned at room temperature of 20 °C in a controlled lab environment. To minimize the effects of temperature and illumination changes, spectral calibration was performed before scanning each sample. We also rotated the sample container and repeated the scans at 0°, 90°, 180°, and 270° to average any variability. As the operating temperature range for the NIR and VIS cameras is −5 °C to

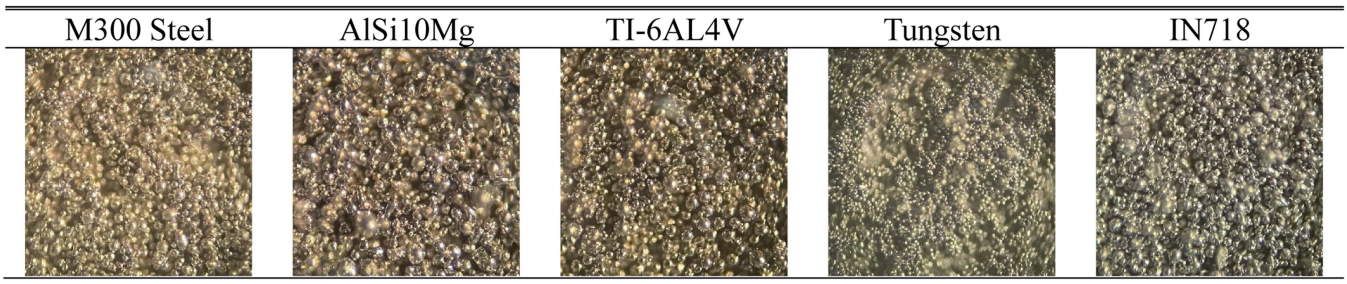


Fig. 4. 100× magnification viewing from apex microscope.

+40 °C and 0 °C to +40 °C, respectively, they worked stably in the controlled environment to produce consistent spectral data in HSI for analysis. In the experiment, five original metal powders were used for training (i.e., building the spectrum dictionary) and mixed metal powders were used for testing. The hypercubes from the four rotation scans of each sample were preprocessed and stacked in a pixelwise manner to produce a stacked image data pool for further processing.

To generate representative spectral samples from the HSI, extraction of the region of interest (ROI) was first applied. This has resulted in approximately 20 000 pixels per sample for the NIR data and 75 000 pixels per sample for the VIS data. To reduce the redundancy and overfitting, we randomly subsampled the ROI pixels with a spacing of $s = M*0.1$, where $M$ is the total number of pixels within the ROI for that sample. This allowed to build representative training and test sets from each category's cube while minimizing the repeated measurements of the same spectral pixels. For example, with 75 000 pixels in the ROI of VIS HSI, we have around 7500 distinct spectral samples per class for training and testing. For robustness, the subsampling stage was repeated ten times to randomly generate ten groups of spectral samples for training and testing, and the averaged testing results are reported for evaluation.

## B. Data Processing

*1) Spectral Calibration:* During the data acquisition stage, the lighting conditions may shift within a hypercube or between different datasets along the scan lines, due possibly to camera quantum and physical configuration differences of the imaging system. To mitigate such an effect, reliable calibrations of the HSI system are required to ensure the stability and acceptance of the data produced. As a result, light calibration is adopted to convert the raw radiance spectrum $s$ to the reflectance spectrum $r$ in order to reduce this incoherence and retain a consistent influence of the light conditions. Without exposing the camera to light, we may get a dark reference spectrum $d$, which estimates the sensor's noise and drift. Then, a white reference spectrum $w$ can be obtained by imaging an ideally reflective white surface (e.g., Spectralon with Lambertian scattering). The normalized light sensitivity of illumination can be obtained as follows:

$$r = \frac{s-d}{w-d}. \tag{1}$$

*2) ROI Extraction:* During the sample preparation, the metal powders are spread out in the round container. After acquiring the HSI data, a robust circle detection method was applied to extract the ROI of the metal powder. This can help to remove the shadow that usually exists near the container boundary, highlighted by a red ring, as shown in Fig. 5(a), while retaining the powder pixels for further analysis.

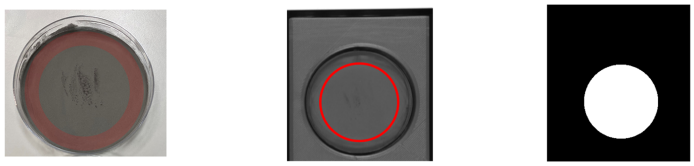


Fig. 5. Illustration of the process for ROI extraction. (a) Image captured by phone. (b) First PCA component from HSI. (c) Selected ROI.

Defining the ROI on a single band was sufficient, as all spectral bands share the identical spatial structure. However, selecting certain band empirically can reduce the scalability of our proposed system. As an uncomplicated and scalable approach, principal component analysis (PCA) is particularly useful for preserving as much of the original variance as possible while reducing the dimensionality of data, while other technique, such as independent component analysis (ICA), is more suitable for separating a multivariate signal into independent sources. Apart from this, PCA has the capability of straightforward computation, interpretability, and widespread implementation. Therefore, the PCA was chosen to compress the high-dimensional HSI data into a primary component image with a much lower dimension yet preserving the dominant spectral variance. The powder pixels can then be separated from the background by thresholding this simplified representation, enabling reliable ROI segmentation.

The steps for circle detection are summarized as follows.

1) Map the HSI data to the feature domain using PCA.
2) Apply an adaptive thresholding method [31] on the first PCA component to extract a binary ROI.
3) Calculate the centroid of the extracted ROI using the central moment, i.e., the mean $(x, y)$ of all white pixels.
4) Determine the minimum radius of the ROI to generate the circular mask, as shown in Fig. 5(b).
5) Apply the ROI mask on the preprocessed hypercube to extract the pixels in a red circle, see in Fig. 5(c).

*3) Band Selection:* To reduce the high dimensionality of the hyperspectral data while retaining its interpretability, we

propose a PRBS method. Unlike feature extraction techniques that project the HSI data into an abstract feature space, band selection identifies a subset of the original spectral bands to preserve the spectral consistency. Our PRBS can retain the most representative bands through the selective elimination of redundant bands.

In PRBS, the only parameter required is the desired number of selected bands *K*. The algorithm then works intrinsically to determine the optimal *K* through an iterative process of clustering and ranking. First, similar spectral bands are merged based on a distance–density metric until *K* distinct clusters emerge. Next, the most representative band in each cluster is selected by ranking the proximities of intracluster bands. This data-driven clustering and ranking automatically identify the top *K* dominant bands from the high-dimensional HSI cube. By retaining the original bands, PRBS maintains the interpretability and spectral consistency while drastically reducing the data volume. The simple tuning of *K* makes the band selection accessible based on application needs. Detailed implementation is presented as follows.

Based on the extracted ROI, a spectral matrix $X \in \Re^{N\times B}$ can be obtained, where *N* is the number of pixel-based spectral vectors and *B* is the number of bands. First, a band hierarchy concept [23] is adopted to group the similar spectral bands iteratively. Let $G = (V, E)$ represents the $X$ in a unidirectional graph, where the node set $V = [1,\ 2, \ldots, B]$ denotes the spectral bands in $X$. Initially, each spectral band is treated as an individual cluster. $E = [e_1, e_2, \ldots, e_Z]$ denotes the distance between two adjacent clusters, where $1 \le Z \le B$. To ensure the computational efficiency during each iteration of the clustering process, it is crucial to use a distance measurement that is both efficient and robust. Therefore, we have opted to utilize the Euclidean distance metric. The distance between the *i*th and the *j*th clusters can be calculated as follows:

$$D_{i,j} = \frac{1}{B}\sqrt{\|X_i - X_j\|^2} = \frac{1}{B}\sqrt{\sum_{n=1}^{N}(X_{n,i} - X_{n,j})^2}. \quad (2)$$

The distance between two adjacent spectral bands can be obtained by setting $e_b = D_{b,b+1}$. If $e_b < e_{b-1}$ and $e_b < e_{b+1}$, band $b$ and band $b + 1$ will be merged into a new cluster $\widehat{X_b}$ that is represented by the mean of all bands it contained. However, considering the noise sensitivity of the Euclidean distance, noisy bands can be clustered separately as they tend to be discriminative against neighboring ones. To address this issue, we further measure the density of each cluster and refine the distance between adjacent clusters $e_b$.

The density of a data cluster refers to the concentration and compactness of the data points within that cluster. In the context of hyperspectral data clustering, we consider the concentration as the number of bands and compactness as the internal distance between each band in the cluster. Therefore, the density $I_b$ for cluster $\widehat{X_b}$ can be obtained as follows:

$$I_b = \ \mathrm{norm}(\widehat{X_b}) * c_b \quad (3)$$

where $\mathrm{norm}(\widehat{X_b})$ represents the Euclidean norm of one cluster, which can be assumed as compactness of $\widehat{X_b}$. $c_b$ is the number of contained bands in the *b*th cluster. Then, $e_b$ will be refined by integrating $I_b$

$$\mathrm{Refined}\ (e_b) = D_{b,b+1} * I_b * I_{b+1}. \quad (4)$$

As a result, a cluster with a lower density will have a shorter distance from its adjacent clusters compared with clusters that have larger densities.

We iteratively apply the merging process above until a defined number of *K* clusters is formed. For efficiently selection of the most representative band from each band cluster, we rank the bands based on their intra proximity (*P*) that is determined by computing their distance to other bands within the same cluster using the chosen metric. Here, we select the Pearson correlation to calculate the *P* for its computationally efficiency. Assuming there are $B'$ bands in the *k*th ($k \in [1, K]$) cluster, the $P$ for the *m*th band in the *k*th cluster can be derived by

$$P_m = \sum_{d=1}^{B'}\left(1 - \frac{\sum\left(X_m - \overline{X_m}\right)\left(X_d - \overline{X_d}\right)}{\sqrt{\sum\left(X_m - \overline{X_m}\right)^2 \sum\left(X_d - \overline{X_d}\right)^2}}\right). \quad (5)$$

Finally, the band with the smallest *P* becomes the dominant one in each cluster, resulting in *K* selected bands for $X$.

## IV. Case Studies and Discussions

In this section, three case studies are used to show the potential of the proposed HIS-based NDT of metal powders, including specific AI techniques introduced in the context.

### A. Case Study 1: Dictionary Building

To precisely characterize the original metal powders, a spectral dictionary is established in this study. Here, we assume that the attributes of the original metal powder spread out in each container are consistent.

*1) Experimental Materials and Settings:* In this study, five categories of original metal powders, including TI-6AL4V, AlSi10Mg, Tungsten, M300 Steel, and IN718, are used to build the spectral dictionary. To evaluate the effectiveness of two spectral dictionaries, we consider this study as a classification problem with the SVM employed for classification. A comparison between VIS spectral dictionary and NIR spectral dictionary is carried out. Overall accuracy (OA), average accuracy (AA), and kappa coefficient (KP) are used for quantitative evaluation

$$\mathrm{OA} = \frac{1}{n}\sum_{i=1}^{T} C_i * 100\% \quad (6)$$

$$\mathrm{AA} = \frac{1}{T}\sum_{i=1}^{T}\frac{C_i}{N_i} * 100\% \quad (7)$$

$$\mathrm{KP} = \left(P_0 - P_e\right) / \left(1 - P_e\right)$$

TABLE II
CLASSIFICATION RESULTS (OA%) WITH MULTIPLE TRAINING PIXELS

| NIR results | | | | | Training pixels | VIS results | | | | |
|---|---|---|---|---|---|---|---|---|---|---|
| CAF | 1DCNN | SAE | SVM-poly | SVM-rbf | | CAF | 1DCNN | SAE | SVM-poly | SVM-rbf |
| 98.09 | 97.19 | 72.44 | 98.68 | 98.85 | 5 | 82.50 | 99.72 | 62.86 | 99.69 | **99.98** |
| 98.71 | 98.75 | 73.14 | 98.78 | 98.95 | 10 | 83.83 | 99.81 | 58.56 | 99.83 | **99.99** |
| 99.37 | 98.98 | 74.75 | 99.06 | 99.11 | 15 | 83.87 | 99.90 | 66.73 | 99.96 | **100.00** |
| 98.97 | 98.93 | 75.07 | 99.22 | 99.24 | 20 | 87.93 | 99.86 | 64.83 | 99.98 | **100.00** |
| 99.30 | 98.84 | 70.28 | 99.26 | 99.26 | 25 | 88.22 | 99.95 | 64.62 | 99.99 | **99.99** |
| 99.59 | 99.03 | 73.91 | 99.40 | 99.46 | 30 | 97.91 | 99.65 | 67.61 | 99.99 | **100.00** |
| 99.58 | 99.70 | 83.04 | 99.81 | 99.84 | 5% | 99.80 | 99.95 | 67.48 | 100.00 | **100.00** |
| 99.78 | 99.86 | 83.52 | 99.88 | 99.90 | 10% | 99.87 | 99.97 | 68.02 | 100.00 | **100.00** |

The best results are highlighted in bold.

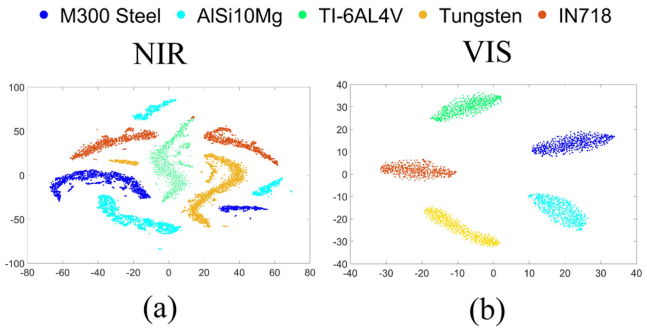


Fig. 6. t-SNE feature space (a, b) of five original samples based on NIR and VIS imagery.

$$P_0 = \text{OA}, P_e = \frac{1}{n^2}\sum_{i=1}^{T}\left(\sum_{j=1}^{T} C_{i,j} * \sum_{j=1}^{T} C_{j,i}\right) \quad (8)$$

where $n$ is the number of observations, $N_i$ are all the pixels in class $i$, the number of observations, $T$ is the number of classes, and $C_i$ represents the number of correctly classified observations in class $i$. $C_{i,j}$ is the row element, and $C_{j,i}$ is the column element in the confusion matrix.

The SVM is selected as the classifier for three reasons:

1) robustness to the Hughes phenomenon and ability to utilize a margin-based criterion [32];
2) wide usage in HSI classification [26];
3) availability of libraries [33] supporting SVMs multiple functions, ensuring simplicity.

Each experiment is repeated ten times, and average results are reported to ensure statistical significance and minimize systematic errors. Disjoint training and testing samples are used within each repetition, with random selecting the number of training pixels (5, 10, 15, 20, 25, 30, 5%, and 10%) in each category.

*2) Results and Discussion:* To assess the discriminative ability of NIR and VIS imagery, t-distributed stochastic neighbor embedding (t-SNE) [34] was utilized to map the spectral bands to a 2-D feature space, as depicted in Fig. 6(a) and (b). Both NIR and VIS imagery have the great discriminability but with different characteristics. NIR imagery exhibits multiple clusters with clear boundaries, whereas VIS spectra tend to organize each sample into distinct clusters in the t-SNE feature space.

To objectively evaluate the effectiveness of our method for dictionary building, we have compared the proposed approach with three deep learning models, i.e., deep 1DCNN [35], stacked autoencoder (SAE) [36], and spectral transformer (CAF) [37] across eight training rates. We fine-tuned these models on our datasets, and the results are given in Tables II –IV. As seen, without sufficient training, all of these deep learning methods underperformed our SVM classifiers on this particular metal powder HSI data. The deep networks may achieve high performance on some public datasets [38], but they required extensive tuning and larger training data to reach parity with SVM on our data. This has suggested that the compared deep learning models may be less effective for our specific application in AM.

Moreover, we have compared two SVM variants, i.e., SVM with the radial basis function kernel (SVM-rbf) and SVM with polynomial kernel (SVM-poly), where the parameters for both kernels are fine-tuned through a grid search. Among the SVM variants, SVM-rbf consistently produced the best results when comparing with SVM-poly, indicating the superiority of the RBF in handling the nonlinearity of the high-dimensional HSI data. Notably, the VIS spectral dictionary with SVM-rbf achieved metrics approaching or reaching 100% in many experiments. In comparison, the NIR dictionary performed worse in terms of OA, AA, and KP. Given these insights, our subsequent experiments will prioritize the VIS spectral dictionary, leveraging the SVM-rbf as the primary model for HSI classification.

## B. Case Study 2: Anomaly Detection

In this study, we assume that HSI is capable of detecting the anomalies in the mixture metal powders, and we take the contamination as a typical scenario.

*1) Experimental Materials and Settings:* To simulate the contamination scenario, eight mixed metal powders were

TABLE III
CLASSIFICATION RESULTS (AA%) WITH MULTIPLE TRAINING PIXELS

| NIR results | | | | | Training pixels | VIS results | | | | |
|---|---|---|---|---|---|---|---|---|---|---|
| CAF | 1DCNN | SAE | SVM-poly | SVM-rbf | | CAF | 1DCNN | SAE | SVM-poly | SVM-rbf |
| 98.02 | 97.08 | 71.83 | 98.67 | 98.85 | 5 | 82.48 | 99.72 | 62.84 | 99.70 | **99.98** |
| 98.72 | 98.78 | 72.83 | 98.75 | 98.94 | 10 | 83.80 | 99.82 | 58.55 | 99.84 | **99.99** |
| 99.37 | 99.01 | 74.26 | 99.06 | 99.12 | 15 | 83.83 | 99.90 | 66.73 | 99.96 | **100.00** |
| 98.98 | 98.96 | 74.59 | 99.22 | 99.24 | 20 | 87.90 | 99.86 | 64.81 | 99.98 | **100.00** |
| 99.30 | 98.87 | 69.76 | 99.26 | 99.26 | 25 | 88.19 | 99.95 | 64.61 | 99.99 | **99.99** |
| 99.58 | 99.06 | 73.46 | 99.39 | 99.46 | 30 | 97.90 | 99.67 | 67.60 | 99.99 | **100.00** |
| 99.57 | 99.70 | 82.65 | 99.81 | 99.84 | 5% | 99.80 | 99.95 | 67.45 | 100.00 | **100.00** |
| 99.78 | 99.86 | 83.15 | 99.88 | 99.90 | 10% | 99.87 | 99.97 | 68.00 | 100.00 | **100.00** |

The best results are highlighted in bold.

TABLE IV
CLASSIFICATION RESULTS (KP∗100) WITH MULTIPLE TRAINING PIXELS

| NIR results | | | | | Training pixels | VIS results | | | | |
|---|---|---|---|---|---|---|---|---|---|---|
| CAF | 1DCNN | SAE | SVM-poly | SVM-rbf | | CAF | 1DCNN | SAE | SVM-poly | SVM-rbf |
| 97.61 | 96.49 | 65.54 | 98.43 | 98.57 | 5 | 78.13 | 99.65 | 53.57 | 99.61 | **99.97** |
| 98.39 | 98.44 | 66.44 | 98.48 | 98.69 | 10 | 79.79 | 99.76 | 48.18 | 99.79 | **99.98** |
| 99.21 | 98.73 | 68.44 | 98.84 | 98.89 | 15 | 79.83 | 99.87 | 58.41 | 99.95 | **100.00** |
| 98.72 | 98.65 | 68.78 | 99.03 | 99.05 | 20 | 84.91 | 99.82 | 56.03 | 99.98 | **100.00** |
| 99.13 | 98.55 | 62.85 | 99.09 | 99.07 | 25 | 85.27 | 99.94 | 55.77 | 99.98 | **99.99** |
| 99.48 | 98.79 | 67.39 | 99.25 | 99.33 | 30 | 97.38 | 99.56 | 59.51 | 99.99 | **100.00** |
| 99.47 | 99.63 | 78.79 | 99.77 | 99.80 | 5% | 99.75 | 99.94 | 59.34 | 100.00 | **100.00** |
| 99.72 | 99.83 | 79.39 | 99.85 | 99.88 | 10% | 99.83 | 99.96 | 60.02 | 100.00 | **100.00** |

The best results are highlighted in bold.

TABLE V
CONTENTS IN EACH MIXED METAL POWDER

| ID | Description | Shaking |
|---|---|---|
| #1 | TI-6AL4V (≥99%) + Tungsten (≤1%) | Yes |
| #2 | IN718 (≥99%) + AlSi10Mg (≤1%) | |
| #3 | M300 Steel (≥99%) + the rest four samples (≤1%) | |
| #4 | AlSi10Mg (≈70%) + IN718 (≈30%) | |
| #5 | Tungsten (≈70%) + TI-6AL4V (≈30%) | |
| #6 | M300 Steel (≈70%) + AlSi10Mg (≈30%) | |
| #7 | TI-6AL4V (≥99%) + Tungsten (≤1%) | No |
| #8 | TI-6AL4V (≈20%) + AlSi10Mg (≈20%) + Tungsten (≈20%) + M300 Steel (≈20%) + IN718 (≈20%). | |

created from five raw samples, see details in Table V, where shaken and unshaken indicate whether or not the container was manually shaken after metal granules were added. After that, we carefully placed the containers to be scanned on the movable system to prevent the secondary powder mixing caused by undesired shaking.

In our study, the identification of contamination is considered an anomaly detection problem. To discover the anomalies within the mixed powders, the VIS spectral dictionary trained by the SVM model in *Case Study 1* will be directly used to detect and recognize the anomalies accordingly.

*2) Results and Discussion:* The anticipated proportion of each type of metal powder in the combined samples is displayed in Table VI. Based on the findings of the #1 and #2 mixed metal powders, it appears that VIS spectral dictionary can provide very promising results in terms of low mean absolute error (MAE) value. For the #3 mixed metal powder, VIS imagery can detect the M300 Steel, AlSi10Mg, and IN718 in this mixed metal powder; however, the estimation of AlSi10Mg and IN718 is far from anticipation.

The initial inference for the misclassification and failure in these three mixed metal powders is given as follows.

1) After shaking the container, two classes of powders are mixed up. The classification performance mainly depends on the way of shaking [see Fig. 7(a)].

TABLE VI
RESULTS OF CASE STUDY 2

| ID | | M300 Steel | AlSi10Mg | TI-6AL4V | Tungsten | IN718 | MAE |
|---|---|---|---|---|---|---|---|
| #1 | *Exp.(%)* | *0.000* | *0.000* | *99.0000* | *1.000* | *0.000* | - |
| | VIS(%) | 0.000 | 0.000 | 99.959 | 0.041 | 0.000 | 0.384 |
| #2 | *Exp.(%)* | *0.000* | *1.000* | *0.000* | *0.000* | *99.000* | - |
| | VIS(%) | 3.108 | 0.004 | 0.179 | 0.000 | 96.709 | 1.315 |
| #3 | *Exp.(%)* | *99.000* | *0.250* | *0.250* | *0.250* | *0.250* | - |
| | VIS(%) | 69.703 | 7.437 | 0.000 | 0.000 | 22.860 | 11.918 |
| #4 | *Exp.(%)* | *0.000* | *70.000* | *0.000* | *0.000* | *30.000* | - |
| | VIS(%) | 0.321 | 96.355 | 0.033 | 0.000 | 3.291 | 10.683 |
| #5 | *Exp.(%)* | *0.000* | *0.000* | *30.000* | *70.000* | *0.000* | - |
| | VIS(%) | 0.000 | 0.000 | 28.181 | 71.819 | 0.000 | 0.727 |
| #6 | *Exp.(%)* | *70.000* | *30.000* | *0.000* | *0.000* | *0.000* | - |
| | VIS(%) | 25.020 | 65.740 | 0.210 | 0.000 | 3.120 | 16.810 |
| #7 | *Exp.(%)* | *0.000* | *0.000* | *99.000* | *1.000* | *0.000* | - |
| | VIS(%) | 0.002 | 4.434 | 86.518 | 1.191 | 7.857 | 4.993 |
| #8 | *Exp.(%)* | *20.000* | *20.000* | *20.000* | *20.000* | *20.000* | - |
| | VIS(%) | 19.170 | 20.483 | 19.700 | 12.558 | 28.088 | 3.429 |

Dominant alloy powder and contamination are highlighted in bold. The excepted portion (Exp.) is presented in italics.

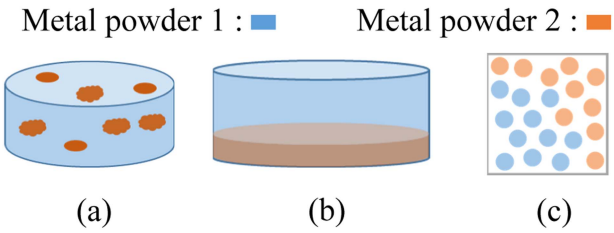


Fig. 7. Illustration of the reasons for misclassification and failure issue. (a) Random spatial distribution. (b) Stratification issue. (c) Spectral mixture in a pixel.

2) In general, large density particles tend to settle in the bottom layer [see Fig. 7(b)], making identification challenging.
3) Single pixels contain two or more classes of powder particles, and the classifier has a low discriminative ability of mixed spectrum [see Fig. 7(c)].

To validate these three assumptions, five more mixed metal powders are generated. For the #4-#6 mixed metal powders, the proportion of contamination was raised to 30%. For the #4 mixed metal powder, VIS imagery can recognize the IN718 as the main contamination, although the estimated proportion is significantly below expectations. For the #5 mixed metal powder, VIS can provide a relatively accurate assessment. For the #6 mixed metal powder, VIS correctly identified M300 Steel and AlSi10Mg but failed to estimate the expected proportions of the predefined metal powders. This discrepancy is likely due to unpredictable spatial distribution hindering precise estimation, as well as spectrum mixing caused by the limited spatial resolution of HSI cameras.

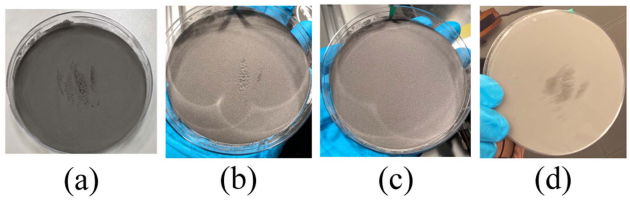


Fig. 8. Surface condition of seventh sample. (a) After sample preparation. (b) After several minutes. (c) In the final state. (d) Bottom condition of seventh sample in the final state.

To mitigate the unpredictable spatial distribution issue, the #7 and #8 samples are generated. For the #7 sample, we first spread the TI-6AL4V over the bottom of the container, then carefully spread tiny portion of Tungsten on top of TI-6AL4V. For eighth sample, five original metal powders are spread over the container in turn. Finally, we placed both containers for scanning without shaking. From the results of the #7 sample, several findings can be concluded. First, VIS imagery can identify TI-6AL4V as the main element and Tungsten as a contamination. Second, misclassification still happens to VIS imagery, which is again caused by spectral mixture issue. Although the container has not been shaken, some TI-6AL4V and Tungsten particles on the surface are still mixed at the pixel level or overlapped by each other, which misleads the classifier to make the wrong estimation. On the other hand, particles with greater density tend to settle at the bottom, Tungsten particles on the surface will be underneath of the TI-6AL4V particles.

As seen in Fig. 8(a), the Tungsten powders are in the middle of the TI-6AL4V powders when they are freshly mixed. In the next few minutes, the majority of the Tungsten particles have sunk through the TI-6AL4V powders, while a few remain on the surface in Fig. 8(b). Eventually, only the TI-6AL4V particles will be visible on the surface, as shown in Fig. 8(c), while the Tungsten granules will completely settle at the bottom of the container, see in Fig. 8(d). This situation may also occur with other samples, such as the #4, simply because the density of IN718 is higher than that of AlSi10Mg, which explains the misclassification from a different perspective. In this case, the issue of spectral mixture no longer exists, but such a condition still brings the difficulty of contamination detection.

For the results from the #8 sample, VIS imagery can well identify the main elements in the same container despite the fact that the estimated portion of each metal powder mismatch the ideal value because of the overlapping issue.

In summary, all these results have actually validated that VIS spectral dictionary is able to recognize the contamination in the mixed metal powder under two preconditions, i.e., metal powders to be characterized need to be on the surface and minimum portion of metal particle needs be larger than a pixel.

*3) Discussion on Shaking Duration and Mixing Sequence:* In Table VII, we compared the results of anomaly detection using four different durations of shaking on the samples #1–#6. As seen, in some cases, longer duration of shaking can actually improve the visibility of the contaminant, such as samples #3 and #4. However, in other cases, such as sample #2, longer shaking may degrade the contaminant visibility. To this end, the

TABLE VII
ANOMALY DETECTION AFTER FOUR DIFFERENT DURATIONS OF SHAKING THE CONTAINER ON SAMPLES #1–6

| ID | | M300 Steel | AlSi10-Mg | TI-6AL4V | Tung-sten | IN718 | MAE |
|---|---|---|---|---|---|---|---|
| #1 | *Exp.(%)* | *0.000* | *0.000* | *99.000* | *1.000* | *0.000* | - |
| | 10 (s) | 0.000 | 0.000 | 99.971 | 0.029 | 0.000 | 0.389 |
| | 20 (s) | 0.000 | 0.000 | 99.988 | 0.012 | 0.000 | 0.395 |
| | 30 (s) | 0.000 | 0.000 | 99.877 | 0.123 | 0.000 | 0.351 |
| | 40 (s) | 0.000 | 0.000 | 99.944 | 0.052 | 0.004 | 0.379 |
| #2 | *Exp.(%)* | *0.000* | *1.000* | *0.000* | *0.000* | *99.000* | - |
| | 10 (s) | 5.297 | 0.562 | 12.259 | 0.000 | 81.883 | 7.022 |
| | 20 (s) | 12.557 | 0.504 | 5.702 | 0.000 | 81.237 | 7.304 |
| | 30 (s) | 5.971 | 0.039 | 17.354 | 0.000 | 76.636 | 9.330 |
| | 40 (s) | 5.219 | 0.052 | 19.900 | 0.000 | 74.830 | 10.047 |
| #3 | *Exp.(%)* | *99.000* | *0.250* | *0.250* | *0.250* | *0.250* | - |
| | 10 (s) | 3.997 | 8.760 | 21.922 | 0.000 | 65.321 | 38.101 |
| | 20 (s) | 7.316 | 16.180 | 11.787 | 0.000 | 64.717 | 36.773 |
| | 30 (s) | 51.660 | 23.402 | 0.003 | 0.000 | 24.936 | 19.135 |
| | 40 (s) | 57.831 | 16.207 | 0.005 | 0.000 | 25.957 | 16.666 |
| #4 | *Exp.(%)* | *0.000* | *70.000* | *0.000* | *0.000* | *30.000* | - |
| | 10 (s) | 9.087 | 88.351 | 0.001 | 0.000 | 2.562 | 10.975 |
| | 20 (s) | 4.962 | 94.342 | 0.000 | 0.000 | 0.696 | 11.722 |
| | 30 (s) | 1.725 | 98.158 | 0.003 | 0.000 | 0.114 | 11.954 |
| | 40 (s) | 2.674 | 75.061 | 0.102 | 0.000 | 22.164 | 3.135 |
| #5 | *Exp.(%)* | *0.000* | *0.000* | *30.000* | *70.000* | *0.000* | - |
| | 10 (s) | 0.003 | 0.000 | 85.599 | 14.393 | 0.006 | 22.243 |
| | 20 (s) | 0.000 | 0.000 | 58.117 | 41.882 | 0.001 | 11.247 |
| | 30 (s) | 0.000 | 0.000 | 80.627 | 19.373 | 0.000 | 20.251 |
| | 40 (s) | 0.000 | 0.000 | 80.126 | 19.874 | 0.000 | 20.050 |
| #6 | *Exp.(%)* | *70.000* | *30.000* | *0.000* | *0.000* | *0.000* | - |
| | 10 (s) | 10.387 | 72.352 | 7.395 | 0.291 | 9.575 | 23.845 |
| | 20 (s) | 11.430 | 72.608 | 4.285 | 1.380 | 10.297 | 23.428 |
| | 30 (s) | 6.524 | 85.501 | 4.235 | 0.420 | 3.320 | 25.390 |
| | 40 (s) | 9.209 | 83.744 | 3.772 | 0.536 | 2.739 | 24.316 |

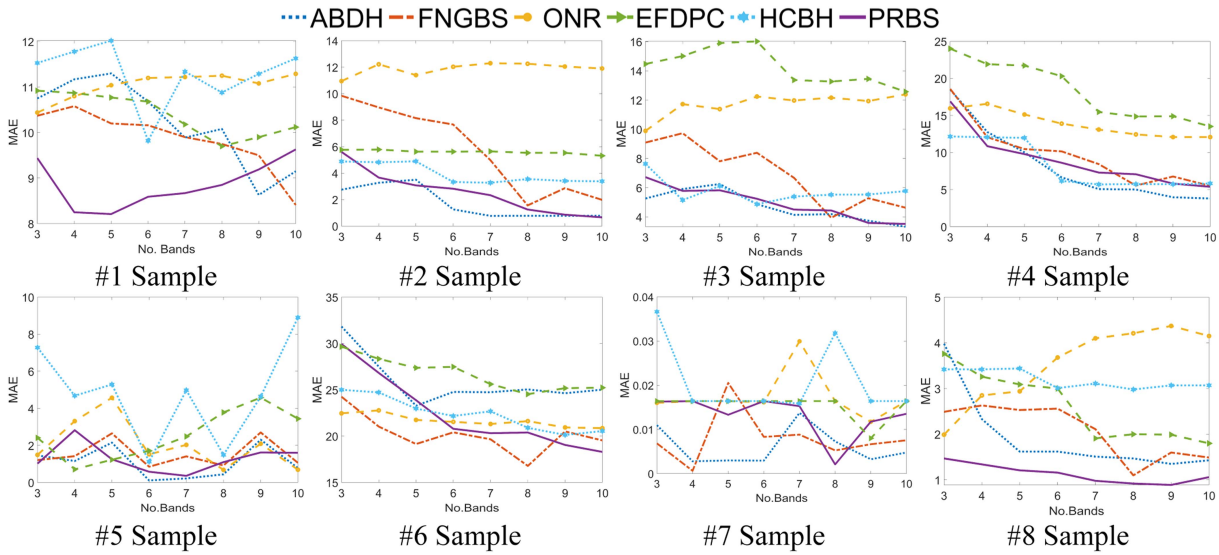


Fig. 9. MAE versus the number of selected bands (no. bands) for six band selection methods evaluated on the eight samples.

relationship between shaking duration and the sample visibility is rather complex, depending on the agitation and particle distribution, e.g., directionality and vigor. While not conclusive, these initial results have demonstrated that there is still no definitive pattern indicating that the detection of contamination is highly dependent on the shaking time. More controlled, systematic agitation can be beneficial for further investigation in the future.

Regarding the mixing sequence, the layer thickness is a key factor that affects the particle visibility after agitation. When it comes to the practical operations in AM, the powder bed thickness is typically less than 100 $\mu$m [39]. With a sufficiently thin-layer distribution of samples, shaking can likely separate and expose various metal powders. However, contaminants buried under thicker layers may still be obscured.

### C. Case Study 3: Band Selection

In this study, we assume that hyperspectral band selection is able to reduce the redundancy in the HSI data while maintaining the contamination detection performance.

*1) Experimental Materials and Settings:* To assess the efficacy of our proposed PRBS band selection method, we compare it with five state-of-the-art (SOTA) band selection approaches, i.e., adaptive distance-based band hierarchy (ADBH) [23], optimal neighborhood reconstruction (ONR) [40], fast neighborhood grouping method (FNGBS)[41], enhanced fast-peak-based clustering (EFDPC) [42], and hyperbolic clustering-based band hierarchy (HCBH) [29]. By taking the full band results from the second case study as a baseline, we compare the detection performance before and after adding these band selection methods in terms of the MAE. A lower MAE value indicates that the selected bands can make the closer estimation of contamination in comparison to use the full spectral bands (baseline).

*2) Results and Discussion:* Fig. 9 compared the band selection results produced by six approaches on the eight samples. Due to the lack of salient features on the spectrum of metal powders, the results from different methods show inconsistency in various samples. For example, the proposed PRBS has the lowest MAE on the #1 and the #8 samples; ADBH has the lowest MAE on the #2 sample, while the MAE of FNGBS is lower than others on the #6 samples. On a different note, more selected bands do not necessarily produce a lower MAE. For example, the MAE of most methods varies with the increasing number of bands on the #5 and #7 samples. The MAE of PRBS reaches the valley when we have only four selected bands; it then increases with the more bands selected for the #1 sample. Although the performance varies with the number of selected bands, the proposed PRBS can produce the best MAE and #2 best standard deviation (STD) on average, indicating its high efficacy and robustness (see Table VIII). Although ONR has a slightly lower STD than our PRBS, its average MAE is twice as high as ours, leading to much inferior efficacy.

Another finding in Fig. 9 is that there is a significant MAE difference when we compare shaking versus no-shaking cases for the category of "TI-6AL4V ($\geq$99%) + Tungsten ($\leq$1%)." This can be explained as follows. Without shaking, the TI-6AL4V is on the bottom layer with the Tungsten visibly on the surface, allowing straightforward detection of them. In contrast, the shaking process changes the present powder distribution, leading to unpredictable mixing and partial occlusion of the Tungsten contaminant. This has increased the heterogeneity in the #1 sample with shaking and reduced the detection accuracy compared with the #7 sample without shaking.

## V. Conclusion and Future Work

In this article, a novel approach was proposed for precision quality control in AM, using hyperspectral image analysis and machine learning. Three case studies were designed to offer unique insights on HSI-based NDT of metal powders-based 3-D printing. Eight mixed samples generated from five categories of original metal powders were employed for modeling and

TABLE VIII
AVERAGED MAE AND ITS ASSOCIATED STD FOR SIX BAND SELECTION METHODS

| Method | ABDH | FNGBS | ONR | EFDPC | HCBH | PRBS |
|---|---|---|---|---|---|---|
| MAE | *3.83* | 4.60 | 6.98 | 6.63 | 4.83 | **3.77** |
| STD | 1.45 | 1.50 | **0.71** | 1.03 | 1.06 | *0.86* |

Best and the second-best results are highlighted in bold and italic, respectively.

validation. The experiments had demonstrated the great value of the integration of machine learning and our band selection in this context, with particularly promising results in characterizing materials and contamination detection.

Some remarkable findings were summarized as follows.

1) Our proposed HSI-based NDT framework can detect the contamination and characterize different mixtures of metal powders at a lower ratio of 1% under two preconditions.
   a) All classes of powder are expected to be visible on the surface.
   b) The particle group is expected to be large enough for capturing at least one pixel of each sample; otherwise, the spectra mixture will heavily affect the classification accuracy.
2) The proposed band selection produces much improved results than other SOTA methods, which is particularly useful to reduce the data redundancy to enable a potential deployment of a multispectral system for reduced cost.

This study represented only the first steps toward developing a robust quality assured solution for AM of metal powders. Significant opportunities remain to build on this foundation through further research, such as to expand the studied contaminant types to validate generalizability beyond the simplified way of powder mixtures. Investigating the impacts of other factors, such as the particle size, shape, porosity, and their resulting optical properties, will also add critical robustness against real-world powder variations. Standardizing the mixing protocols could help to improve the characterization of layered or clumped particles, even supported by the spectral unmixing techniques. By tackling these limitations via rigorous follow-on studies, a more comprehensive solution can be built to satisfy industrial needs in metal AM.

## REFERENCES


[1] J. Baldwin, "3D printing trends: 2021 predictions," Accessed on: May 30, 2023. [Online]. Available: https://blog.grabcad.com/blog/2021/02/10/3d-printing-trends-2021-predictions/

[2] G. Jacob, G. Jacob, C. U. Brown, M. A. Donmez, S. S. Watson, and J. Slotwinski, "Effects of powder recycling on stainless steel powder and built material properties in metal powder bed fusion processes," US Dept. Commerce, Nat. Inst. Standards Technol., Gaithersburg, MD, USA, 2017.

[3] G. Shanbhag and M. Vlasea, "Powder reuse cycles in electron beam powder bed fusion—Variation of powder characteristics," *Materials*, vol. 14, no. 16, 2021, Art. no. 4602.

[4] R. Williams, M. Bilton, N. Harrison, and P. Fox, "The impact of oxidised powder particles on the microstructure and mechanical properties of Ti-6Al-4 V processed by laser powder bed fusion," *Additive Manuf.*, vol. 46, 2021, Art. no. 102181.

[5] S. Liu and Y. C. Shin, "Additive manufacturing of Ti6Al4V alloy: A review," *Mater. Des.*, vol. 164, 2019, Art. no. 107552.

[6] A. Yadollahi and N. Shamsaei, "Additive manufacturing of fatigue resistant materials: Challenges and opportunities," *Int. J. Fatigue*, vol. 98, pp. 14–31, 2017.

[7] V. B. Vukkum and R. K. Gupta, "Review on corrosion performance of laser powder-bed fusion printed 316L stainless steel: Effect of processing parameters, manufacturing defects, post-processing, feedstock, and microstructure," *Mater. Des.*, vol. 221, 2022, Art. no. 110874.

[8] D. L. Prakash, M. Walsh, D. Maclachlan, and A. Korsunsky, "Crack growth micro-mechanisms in the IN718 alloy under the combined influence of fatigue, creep and oxidation," *Int. J. Fatigue*, vol. 31, no. 11/12, pp. 1966–1977, 2009.

[9] H. Rao, S. Giet, K. Yang, X. Wu, and C. H. Davies, "The influence of processing parameters on aluminium alloy A357 manufactured by selective laser melting," *Mater. Des.*, vol. 109, pp. 334–346, 2016.

[10] L. E. Thomas-Seale, J. C. Kirkman-Brown, M. M. Attallah, D. M. Espino, and D. E. Shepherd, "The barriers to the progression of additive manufacture: Perspectives from U.K. industry," *Int. J. Prod. Econ.*, vol. 198, pp. 104–118, 2018.

[11] K. A. Mumtaz, P. Erasenthiran, and N. Hopkinson, "High density selective laser melting of Waspaloy," *J. Mater. Process. Technol.*, vol. 195, no. 1/3, pp. 77–87, 2008.

[12] S. A. Shevchik, G. Masinelli, C. Kenel, C. Leinenbach, and K. Wasmer, "Deep learning for in situ and real-time quality monitoring in additive manufacturing using acoustic emission," *IEEE Trans. Ind. Inform.*, vol. 15, no. 9, pp. 5194–5203, Sep. 2019.

[13] S. Di Cataldo et al., "Optimizing quality inspection and control in powder bed metal additive manufacturing: Challenges and research directions," *Proc. IEEE*, vol. 109, no. 4, pp. 326–346, Apr. 2021.

[14] A. Lopez, R. Bacelar, I. Pires, T. G. Santos, J. P. Sousa, and L. Quintino, "Non-destructive testing application of radiography and ultrasound for wire and arc additive manufacturing," *Additive Manuf.*, vol. 21, pp. 298–306, 2018.

[15] Y. Chen, X. Peng, L. Kong, G. Dong, A. Remani, and R. Leach, "Defect inspection technologies for additive manufacturing," *Int. J. Extreme Manuf.*, vol. 3, no. 2, 2021, Art. no. 022002.

[16] N. Sanaei and A. Fatemi, "Defects in additive manufactured metals and their effect on fatigue performance: A state-of-the-art review," *Prog. Mater. Sci.*, vol. 117, 2021, Art. no. 100724.

[17] M. Y. Kayacan and N. Yılmaz, "An investigation on the measurement of instantaneous temperatures in laser assisted additive manufacturing by thermal imagers," *Measurement*, vol. 160, 2020, Art. no. 107825.

[18] P. J. Withers et al., "X-ray computed tomography," *Nature Rev. Methods Primers*, vol. 1, no. 1, pp. 1–21, 2021.

[19] A. Du Plessis, I. Yadroitsava, and I. Yadroitsev, "Effects of defects on mechanical properties in metal additive manufacturing: A review focusing on X-ray tomography insights," *Mater. Des.*, vol. 187, 2020, Art. no. 108385.

[20] A. Thompson, I. Maskery, and R. K. Leach, "X-ray computed tomography for additive manufacturing: A review," *Meas. Sci. Technol.*, vol. 27, no. 7, 2016, Art. no. 072001.

[21] S. Romano, A. Abel, J. Gumpinger, A. D. Brandão, and S. Beretta, "Quality control of AlSi10Mg produced by SLM: Metallography versus CT scans for critical defect size assessment," *Additive Manuf.*, vol. 28, pp. 394–405, 2019.

[22] P. Wang et al., "Scanning optical microscopy for porosity quantification of additively manufactured components," *Additive Manuf.*, vol. 21, pp. 350–358, 2018.

[23] H. Sun et al., "Adaptive distance-based band hierarchy (ADBH) for effective hyperspectral band selection," *IEEE Trans. Cybern.*, vol. 52, no. 1, pp. 215–227, Jan. 2022.

[24] Y. Fu et al., "An overview of crop nitrogen status assessment using hyperspectral remote sensing: Current status and perspectives," *Eur. J. Agron.*, vol. 124, 2021, Art. no. 126241.

[25] S. Peyghambari and Y. Zhang, "Hyperspectral remote sensing in lithological mapping, mineral exploration, and environmental geology: An updated review," *J. Appl. Remote Sens.*, vol. 15, no. 3, 2021, Art. no. 031501.

[26] Y. Yan, J. Ren, J. Tschannerl, H. Zhao, B. Harrison, and F. Jack, "Non-destructive phenolic compounds measurement and origin discrimination of peated barley malt using near-infrared hyperspectral imagery and machine learning," *IEEE Trans. Instrum. Meas.*, vol. 70, May 2021, Art. no. 5010715.
[27] Y. Yan et al., "Non-destructive testing of composite fiber materials with hyperspectral imaging—Evaluative studies in the EU H2020 FibreEUse project," *IEEE Trans. Instrum. Meas.*, vol. 71, Mar. 2022, Art. no. 6002213.
[28] J. Zabalza et al., "Hyperspectral imaging based corrosion detection in nuclear packages," *IEEE Sensors J.*, vol. 23, no. 21, pp. 25607–25617, Nov. 2023.
[29] H. Sun, L. Zhang, J. Ren, and H. Huang, "Novel hyperbolic clustering-based band hierarchy (HCBH) for effective unsupervised band selection of hyperspectral images," *Pattern Recognit.*, vol. 130, 2022, Art. no. 108788.
[30] E. Bertino, S. Merrill, A. Nesen, and C. Utz, "Redefining data transparency: A multidimensional approach," *Computer*, vol. 52, no. 1, pp. 16–26, 2019.
[31] D. Bradley and G. Roth, "Adaptive thresholding using the integral image," *J. Graph. Tools*, vol. 12, no. 2, pp. 13–21, 2007.
[32] J. Zabalza et al., "Novel two-dimensional singular spectrum analysis for effective feature extraction and data classification in hyperspectral imaging," *IEEE Trans. Geosci. Remote Sens.*, vol. 53, no. 8, pp. 4418–4433, Aug. 2015.
[33] C.-C. Chang and C.-J. Lin, "LIBSVM: A library for support vector machines," *ACM Trans. Intell. Syst. Technol.*, vol. 2, no. 3, 2011, Art. no. 27.
[34] L. van der Maaten and G. Hinton, "Visualizing data using t-SNE," *J. Mach. Learn. Res.*, vol. 9, no. 11, pp. 2579–2605, 2008.
[35] W. Hu, Y. Huang, L. Wei, F. Zhang, and H. Li, "Deep convolutional neural networks for hyperspectral image classification," *J. Sensors*, vol. 2015, 2015, Art. no. 258619.
[36] L. Windrim, R. Ramakrishnan, A. Melkumyan, R. J. Murphy, and A. Chlingaryan, "Unsupervised feature-learning for hyperspectral data with autoencoders," *Remote Sens.*, vol. 11, no. 7, 2019, Art. no. 864.
[37] D. Hong et al., "SpectralFormer: Rethinking hyperspectral image classification with transformers," *IEEE Trans. Geosci. Remote Sens.*, vol. 60, Nov. 2021, Art. no. 5518615.
[38] Y. Wen, M. F. Rahman, H. Xu, and T.-L. B. Tseng, "Recent advances and trends of predictive maintenance from data-driven machine prognostics perspective," *Measurement*, vol. 187, 2022, Art. no. 110276.
[39] X. Zhang and F. Liou, "Introduction to additive manufacturing," in *Additive Manufacturing*. Amsterdam, The Netherlands: Elsevier, 2021, pp. 1–31.
[40] Q. Wang, F. Zhang, and X. Li, "Hyperspectral band selection via optimal neighborhood reconstruction," *IEEE Trans. Geosci. Remote Sens.*, vol. 58, no. 12, pp. 8465–8476, Dec. 2020.
[41] Q. Wang, Q. Li, and X. Li, "A fast neighborhood grouping method for hyperspectral band selection," *IEEE Trans. Geosci. Remote Sens.*, vol. 59, no. 6, pp. 5028–5039, Jun. 2021.
[42] S. Jia, G. Tang, J. Zhu, and Q. Li, "A novel ranking-based clustering approach for hyperspectral band selection," *IEEE Trans. Geosci. Remote Sens.*, vol. 54, no. 1, pp. 88–102, Jan. 2016.

**Yijun Yan** (Member, IEEE) received the Ph.D. degree in electronic and electrical engineering from the University of Strathclyde (UoS), Glasgow, U.K., in 2018.

After Ph.D., he was a Postdoctor with UoS and Robert Gordon University. He currently holds the position of Lecturer in computing with the School of Science and Engineering, University of Dundee, Dundee, U.K., alongside an honorary Lecturer with Robert Gordon University, Aberdeen, U.K. His research primarily focuses on pattern recognition, hyperspectral imagery, and their application in remote sensing, as well as nondestructive testing across diverse industrial environments.

**Jinchang Ren** (Senior Member, IEEE) received the Ph.D. degree in electronic imaging from the University of Bradford, Bradford, U.K., in 2009.

He is currently a Professor of computing science with Robert Gordon University (RGU), Aberdeen, U.K. He is the Transparent Ocean Lead and the Director of the Hyperspectral Imaging (HSI) Lab, National Subsea Centre, RGU, Aberdeen, U.K., working on multimodal sensing-based inspection and condition monitoring of marine/energy infrastructures and ocean environments. His research interests include HSI, image processing, computer vision, big data analytics, and machine learning.

**He Sun** received the Ph.D. degree in electronic and electrical engineering from the University of Strathclyde, Glasgow, U.K., in 2020.

He is an Assistant Professor with the Key Laboratory of Computational Optical Imaging Technology, Aerospace Information Research Institute, Chinese Academy of Sciences, Beijing, China. His research interests include hyperspectral target detection and band selection.

**Robert Williams** received the Ph.D. degree in powder metallurgy from the University of Liverpool, Liverpool, U.K., in 2021.

He is currently the Lead Metallurgist for carpenter additive Liverpool manufacturing processes. He leads the implementation of new technology and the optimization of atomization processes to develop current and new materials for the additive manufacturing sector. He is the Carpenter Additive Technical Lead for GRCop42 and has a research interest in new alloy development and material characterization technology for reactive alloys.